Applied Surface Science 492 (2019) 896–908

Contents lists available at ScienceDirect

Applied Surface Science

journal homepage: www.elsevier.com/locate/apsusc

Full length article

Improved surface charge storage properties of *Prosopis juliflora* (*pods*) derived onion–like porous carbon through redox-mediated reactions for electric double layer capacitors

Sathyanarayanan Shanmugapriya[a], Subramani Surendran[a], Yun Sung Lee[b], Ramakrishnan Kalai Selvan[a,*]

[a] Energy Storage and Conversion Devices Laboratory, Department of Physics, Bharathiar University, Coimbatore 641-046, Tamil Nadu, India
[b] Department of Chemical Engineering, Chonnam National University, Gwangju 61186, Republic of Korea

ARTICLE INFO

Keywords:
Prosopis juliflora
Onion–like porous carbon
Redox-additive
Electric double layer capacitor

ABSTRACT

Turning trash into treasure, the present work divulges the preparation of onion-like porous carbon derived out of the most malignant invasive weed, the *Prosopis juliflora*. The pods of the *Prosopis juliflora* are treated hydrothermally and chemically activated using KOH. The effect of activation temperature on the pore formation is investigated to obtain the desired porous carbon. The prepared porous carbon (J–800) has a significant specific surface area of 967 $m^2 g^{-1}$ with unique morphology of onion-like nanostructures and provided a sensible specific capacitance of 274 F g^{-1} at 1.3 A g^{-1} in H_2SO_4 electrolyte. Further, the performance of the device is effectually enhanced by adding KI as redox additive. Interestingly, the increased cell voltage (1.4 V) and improved cell capacitance of 588 F g^{-1} is obtained. Ultimately, a superior energy density of 35.7 Wh kg^{-1} at an enhanced power density of 971 W kg^{-1} is also obtained in the redox additive based aqueous electrolyte. A detailed investigation of the surface storage mechanism is discussed, and the stability of the prepared supercapacitors is also demonstrated. Thus, the most eradicable eco-threat *P. juliflora* is successfully reformed into an efficient electrode material for the energy storage application.

1. Introduction

The inevitable reliance on overpriced fossil fuels and their malicious impact on the environment has allegedly forced us to hunt the low-cost and green sources of energy. Also, the contemporary craving for uninterrupted supply and efficient storage of energy has urged the use of electrochemical energy as an alternative power source. Among such electrochemical energy storage systems, the electric double-layer capacitors (EDLCs) always have an imperative role since they provide higher power density (> 10 kW kg^{-1}), very rapid charging/discharging capability or power capability and significantly longer cycle life (> 50,000 cycles). The main limitation of EDLCs is their lower energy density (< 10 Wh kg^{-1} in aqueous medium) than batteries combined with a high cost per unit energy [1–3]. The energy storage mechanism of EDLCs is based on the adsorption of electrolyte ions and the formation of an electric double layer on the electrode/electrolyte interface [4,5]. Various carbon-based materials such as graphite [6,7], graphene [8,9], activated carbons (ACs) [10,11], carbon nanotubes [12,13], carbon nanofibers [14,15], carbon aerogels [16,17] and carbide-derived carbons [18,19] have been investigated as electrode materials because of their good conductivity and high surface area. As well as, the recent works indicated that hierarchical porous carbon and high N/O doped porous carbon displayed excellent electrochemical performances for supercapacitors [20–23].

Moreover, activated carbons are widely used because of their well-developed surface area, high porosity, good accessibility for electrolyte ions, and high chemical and electrochemical stability [24–26]. Commercial grades of activated carbon are manufactured from bituminous coal, peat and lignite, which are quite expensive. Thus, it is to be stressed that obtaining porous carbon through biomass wastes is comparatively cheap, and hence, it is considered as a potential raw material for the preparation of porous carbons [27]. *Prosopis juliflora*, the most intransigent invasive weed, has colonized millions of hectares of land and are depleting the water resources, threatening the crop production, and displacing native flora and fauna [28]. The eradication of this eco-threat appears to be challenging and ungovernable. Therefore the knack of employing alternate management is that it can be converted into a productive, profitable, and sustainable resource for energy sectors,

* Corresponding author.
E-mail address: selvankram@buc.edu.in (R.K. Selvan).

https://doi.org/10.1016/j.apsusc.2019.06.147
Received 3 May 2019; Received in revised form 7 June 2019; Accepted 13 June 2019
Available online 15 June 2019

especially activated carbon production [29]. Moreover, there were only a few reports on *P. juliflora* derived carbon for the energy storage applications; which include the preparation of tube-like carbon as electrode material for the fabrication of non-aqueous Li-ion hybrid supercapacitors [30–32].

As mentioned earlier, the most important drawback of EDLCs is the lower energy density. Normally, the energy density can be enhanced by two approaches, (i) increasing the specific capacitance and (ii) increasing the operating voltage of the device. Hence the specific capacitance can be enhanced by improving the conductivity, tuning the porosity, incorporating the surface functional groups and increasing the specific surface area of the electrode material [33]. On the other hand, for increasing the operating voltage, the electrolytes are altered by hosting the redox species, which generates faradaic pseudocapacitance that contributes to the overall capacitance, which in turn high energy density. Among the above two processes, the redox-mediated process is relatively simple and effective [34–39]. As well as the redox-additive liquid electrolyte overcomes the common issues such as low accessibility, poor ionic mobility, and surface wettability between the electrode and electrolyte [40]. Different materials have been used as redox additives, such as KI, $K_3Fe(CN)_6$, $K_4Fe(CN)_6$, KBr, $FeBr_3$, hydroquinone, *p*-phenylenediamine, etc. with conventional electrolytes like KOH, H_2SO_4, Na_2SO_4, and so on [41]. Among the redox elements, the iodine appears to be impeccable because of its rich oxidation states from the most stable iodide (−1) to iodate (+5). Previously, the exceptional electrochemical behaviour of carbon/iodide interface has been successfully demonstrated [42–47], as iodide (I) can produce redox pairs such as $3I/I_3$, $2I/I_2$, $2I_3/3I_2$ and I_2/IO_3 during the electrochemical process. Due to the small ionic sizes (around 0.5 to 1.5 nm), these redox derived polyiodides can easily access the micropores and small mesopores of the porous electrodes and hence it is proved to be one of the most compatible redox additives for the activated carbon-based electrodes having hierarchical porous network [42–44]. Moreover, there are no reports for the redox additive mediated electrochemical activity of *P. juliflora* derived carbon to the best of our knowledge.

In the present work, the preparation of onion-like porous carbon from the *P. juliflora* pods is reported for the application of supercapacitors. Moreover, the retarded energy density of EDLC is addressed with the redox additive based aqueous electrolyte. Initially, the desired porous structure is attained by optimizing the activation temperature. Then the optimized electrode (J–800) with the well-defined porous network is employed for EDLC fabrication after a detailed physiochemical characterization. Further, the performance of the resulting device is improved by modifying the electrolyte with the use of KI as redox additive. Moreover, the detailed surface charge storage mechanism behind the enhancement of energy density with the use of redox additive is discussed. Hence, this work is strongly believed to be an alternate management or control-technology for the eradication of the most environmentally threatening invasive weed *P. juliflora*.

2. Materials and methods

2.1. Source of porous carbon

The porous carbon used in this study was obtained from the pods of *P. juliflora* trees colonized in the dried water body of Sathyamangalam town (11.5048° N, 77.2384° E) in Tamilnadu, India. The pods were collected, sun-dried and ground coarsely. Subsequently, it was oven dried at 80 °C for 24 h and again ground to obtain a fine powder which was used as raw material for the preparation of porous carbon.

2.2. Synthesis of porous carbon

The finely powdered pods of *P. juliflora* was taken in a quantity of 2 g along with 40 ml of 1 M H_2SO_4 in a Teflon lined autoclave and placed at 180 °C for 24 h. The collected hydrothermal carbon (HTC) was washed with double distilled (DD) water followed by ethanol and dried at 80 °C for 12 h. The obtained HTC was soaked with KOH at a ratio of 1:1 using DD water and kept under stirring for 24 h. The resultant was coarsely ground and dried overnight at 80 °C. Further, the obtained KOH activated HTC was carbonized at three different temperatures of 600, 700 and 800 °C for 1 h under an argon atmosphere at a heating rate of 10 °C/min. An appropriate quantity of 1 M HCl was added separately to all the three carbonized samples and washed thoroughly with DD water and ethanol to bring a neutral pH. Later, the samples were dried overnight at 80 °C to get the desired porous carbons that were named as J-600, J-700, and J-800 based on their carbonization temperature.

2.3. Characterization of porous carbon

X-ray diffraction (XRD) patterns were obtained from a diffractometer (Model: Rint 1000, Rigaku, Japan) using Cu K_α radiation (λ = 0.15418 nm) in the 2 θ range of 10° to 80°. Fourier transform infrared (FTIR) spectra of the samples were recorded by an IR Prestige-21 spectrometer (Schimadzu Corp., Japan) with the scan range of 400–4000 cm^{-1}. The Raman spectra were performed using HORIBA Jobin Yvon LabRAM HR 800. Scanning Electron Microscope (Model S-4700, Hitachi, Japan) was used to investigate the surface morphology of the carbons. The Brunauer–Emmett–Teller (BET) specific surface area and pore size distribution were determined by conducting a nitrogen adsorption/desorption analysis recorded at 77 K using ASAP 2420 device from Micromeritics®. X-ray photoelectron spectroscopy, XPS was also performed using a Multilab 2000 (Thermo Scientific, UK) with monochromator and Al K_α radiation ($h\nu$ = 1486.6 eV). The distinct lattice fringes and selected area electron diffraction, SAED pattern were recorded using a JEOL JEM 2100 high-resolution transmission electron microscope.

2.4. Electrode preparation and cell assembly

The working electrodes were fabricated by finely mixing the prepared porous carbon (8 mg) with carbon black (1 mg) and poly-(vinylidene fluoride) (PVDF, 1 mg) in 0.3 ml of *N*-methyl-2-pyrrolidone (NMP) to produce a homogeneous slurry. Then an appropriate amount of mixture was coated on a pre-treated flexible carbon cloth substrate (1 cm × 1 cm) using a paintbrush to attain a mass loading of ~1 mg. Finally, the fabricated electrodes were dried at 80 °C in vacuum for 24 h. The symmetric supercapacitors were assembled using the prepared porous carbon electrodes, separated by a polypropylene sheet immersed in 0.5 M H_2SO_4 and 0.5 M H_2SO_4 + 0.05 M KI, electrolytes.

2.5. Electrochemical measurements

The electrochemical measurements were carried out using Bio-Logic SP150 instrumentation at room temperature. The fundamental electrochemical characterizations involving the three-electrode system were done using graphite rod and Ag/AgCl as counter and reference electrodes, respectively. All the three-electrode studies were obtained using 0.5 M H_2SO_4 electrolyte. The electrochemical impedance spectroscopy (EIS) measurements were made by applying an AC voltage of 10 mV amplitude in the frequency range of 1 Hz to 1 MHz at open circuit voltage (OCV). Further, the cyclic voltammetry (CV) and galvanostatic charge-discharge (GCD) tests were done in the potential range of 0 to 0.8 V at various scan rates (5–50 mV s^{-1}) and current densities (0.6 to 6.3 A g^{-1}), respectively. The specific capacitance of the electrodes is calculated using the following equations (Eqs. (1) & (2)),

$$C_{sp} = \frac{\int IdV}{m \times \vartheta \times \Delta V} \quad (1)$$

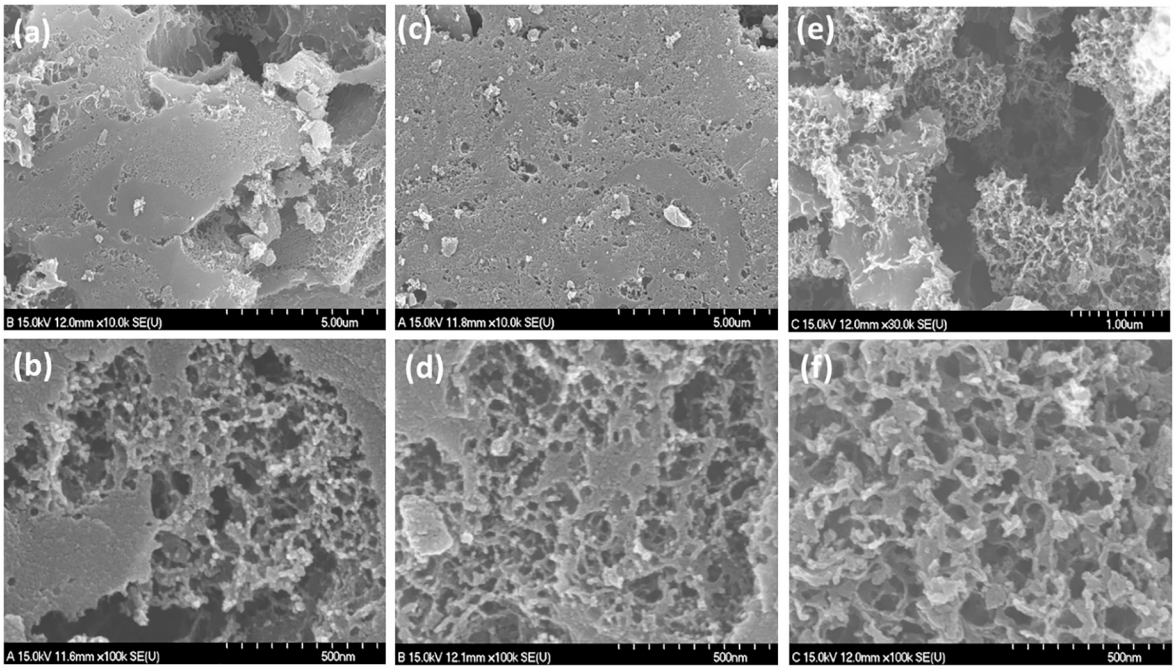

Fig. 1. FESEM micrographs of (a, b) J–600, (c, d) J–700 and (e, f) J–800 porous carbons.

$$C_{sp} = \frac{I \times \Delta t}{m \times \Delta V} \tag{2}$$

where, $\int IdV$ is the integral area of the CV curve, m is the mass of a single electrode, ϑ is the applied scan rate, ΔV is potential range, I is the applied current, and Δt is the discharge current. The specific capacitance of the device (C_{sp}), energy density (E) and power density (P) are obtained using the equations, Eqs. (3)–(5).

$$C_{sp} = 4\,\frac{I \times \Delta t}{M \times \Delta V} \tag{3}$$

$$E = \frac{1000\, I \int V(t)dt}{3600\, M} \tag{4}$$

$$P = \frac{3600\, E}{\Delta t} \tag{5}$$

Here, the M is the total mass of the two electrodes and $I\int V(t)dt$ is the integral area of the discharge curve.

3. Results and discussion

3.1. Morphological and textural characteristics of porous carbon

The morphological features of the prepared porous carbons are studied using FESEM and TEM micrographs. Fig. 1a, b shows the FESEM images of J-600, which demonstrates the poor distribution of porous morphology due to the inadequate temperature for the complete activation and pore formation. While further increasing the activation temperature to 700 °C, the pore formation is about to report an even distribution but without any prominence (Fig. 1c, d). Therefore, the activation temperature was further increased to 800 °C to achieve a comprehensive activation with synchronized pore distribution. Interestingly, the desired porous carbon with uniform porous texture is attained at 800 °C (Fig. 1e, f). It can also be seen that the sample possesses a rich interconnected porous structure that offers tunnel like provisions to access the inner surface of the material. Thus, the obtained porous structured J–800, is anticipated to provide better electrochemical properties.

The effect of activation temperature on the evolution of porous texture is explained using the schematic representation (Scheme 1) for better understanding. The generation of the porous network in the prepared carbons follow the conventional KOH activation process [48,49]. At ~600 °C, the KOH is completely reacted with carbon to form K_2CO_3 (Step: 1). Due to the low activation temperature, the complete decomposition of K_2CO_3 is not possible; therefore the formation of pores in J–600 is not certain over the entire portion, and hence it exhibits poor porous structure. Consequently, at 700 °C activation, the decomposition of K_2CO_3 is improved (Step: 2), which results in the random distribution of obscure pores in J–700 [50]. On the other hand, the potassium compounds are completely reduced to metallic K (Step: 3) at the activation temperature of 800 °C. In addition to this chemical activation, physical activation also occurs through gasification and supports the further development of porosity [51]. Thus, the activated carbon with the desired hierarchical porous structure is attained at a reasonably high temperature of 800 °C.

To further get an insight into the morphological features of prepared porous carbons, a representative transmission electron microscopic study was carried out for J–800 and the obtained results are provided in Fig. 2(a–c). The TEM analysis transpires the onion-like carbon nanostructures of the prepared J–800. The onion-like nanostructures (OLNs) are observed with polyhedral shape, hollow core, multiple shells and smaller size < 100 nm satisfying the morphological features of “carbon onions” [52]. The average width of the outer shells of OLNs is measured to be around ~3 nm, and the outer shells are found to get overlapped with one another to form clusters of onion ring pattern. This connection of OLNs makes them better conductive by reducing the resistance between the neighbouring particles.

The electrochemical performance of carbon material is generally determined by its electrolyte-accessible specific surface area (SSA) and the pore structure. Thus, to get a better understanding on the nature of attained porosity, the SSA and pore size distribution of the prepared porous carbons were examined using the BET analysis, and the obtained results are provided in Fig. 3. Fig. 3a shows the N_2 adsorption-desorption isotherms of the prepared porous carbons. The obtained isotherms belong to the type IV combined with type I features (IUPAC classification). The isotherms exhibit a strong adsorption at low pressure ($P/P_0 < 0.01$) followed by a broadening knee along a hysteresis loop in the midrange ($0.2 < P/P_0 < 0.4$) and a slight upward tendency at relative-high pressure ($P/P_0 = 0.9–1.0$) reporting the

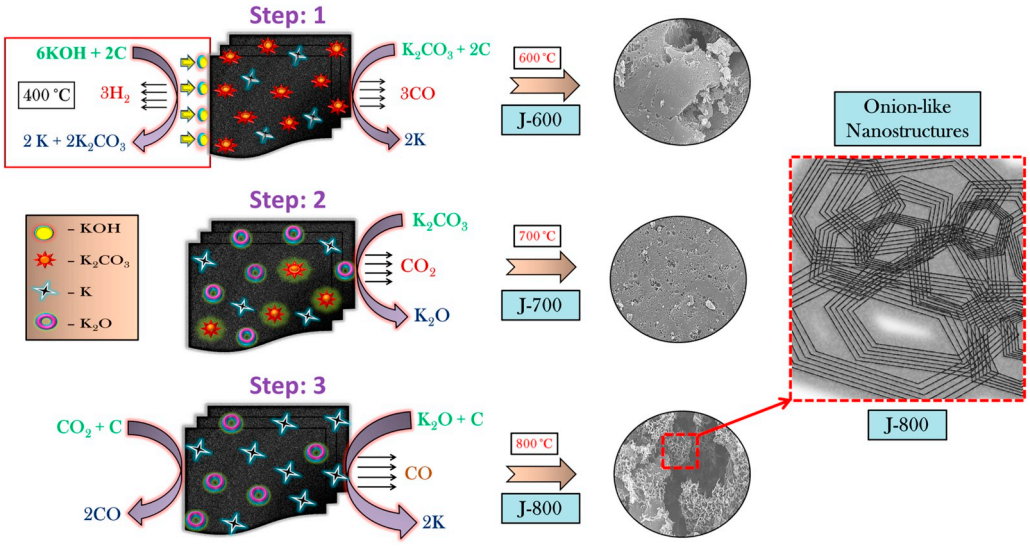

Scheme 1. Effect of activation temperature on the evolution of porous structure.

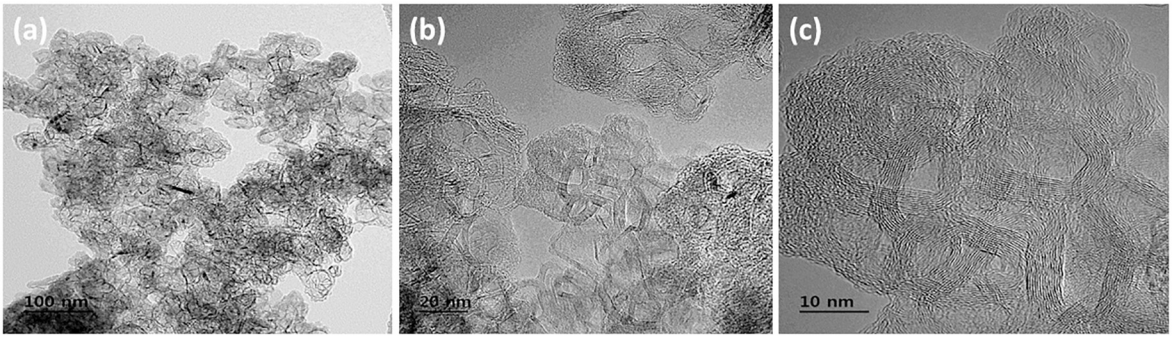

Fig. 2. (a–c) TEM micrographs of J–800.

hierarchical porous network of prepared porous carbons with all the three micro, meso and macropores, respectively [20,21,53,54]. The textural parameters calculated from the BET analysis are provided in Table 1. Among the prepared carbons, the J–800 has demonstrated a high specific surface area of about 967 $m^2 g^{-1}$ than J–600 (503 $m^2 g^{-1}$) and J–700 (610 $m^2 g^{-1}$). Similarly, J–800 possesses higher pore volume of 0.53 $cm^3 g^{-1}$ than J–600 and J–700. The average pore diameter of the prepared porous carbons is found to be ~4 nm. Thus, the majority of pores obtained are either smaller mesopores or micropores. Using t-plot method the microporous surface area and micropore volume are calculated, which shows that the J–800 provides the maximum value of 849 $m^2 g^{-1}$ and 0.3 $cm^3 g^{-1}$, respectively. Overall, the pore volume of micropores increases with increasing activation temperature.

Fig. 3b shows the pore size distribution of the prepared porous carbons obtained from DFT method. The hierarchical porous network is further validated according to the pore size distribution (Table 1). It can be seen that the J–800 shows a relatively narrow distribution with maximum peaks at < 2 nm and ~25 nm corresponding to the

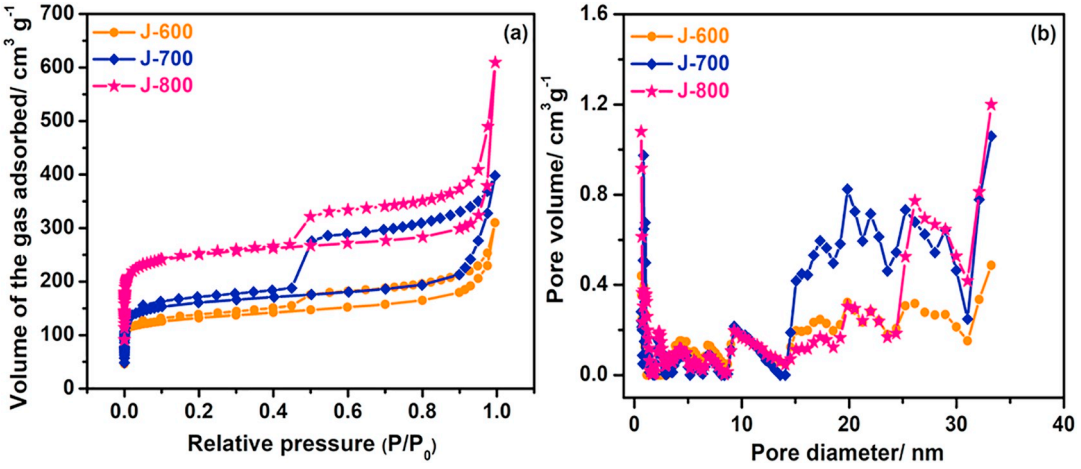

Fig. 3. (a) N_2 adsorption-desorption isotherms and (b) pore size distributions of porous carbons.

Table 1
Textural parameters of the porous carbons.

Carbon	BET surface area ($m^2 g^{-1}$)	Pore volume ($cm^3 g^{-1}$)	Pore diameter (nm)	Microporous surface area ($m^2 g^{-1}$)	Micropore volume ($cm^3 g^{-1}$)
J-600	503	0.325	3.811	391	0.155
J-700	610	0.462	4.032	500	0.201
J-800	967	0.527	3.897	846	0.336

micropores and mesopores, respectively. Normally, these micropores significantly assist the double-layer formation in EDLCs, while mesopores serve as reservoirs for charge storage [55,56]. Therefore, the developed pore system of J–800 will provide sufficient charge storage through electric double-layer formation, and the interconnected porous network will act as channels to support faster transport of ions and electrons.

3.2. Physiochemical properties of porous carbon

The X-ray diffraction patterns (Fig. 4a) of all the prepared porous carbons are similar, and the observed two significant peaks at the 2θ values of 24° and 43°, corresponds to the (002) and (100/101) *h k l* planes of carbon, respectively. In particular, a broad peak at 24° corresponds to the typical reflection of graphitic carbon and a weak broad peak at 43° corresponds to the turbostratic stacking of hexagonal layers of carbon atoms indicating the presence of amorphous carbon [57]. The calculated d-spacing of the prepared porous carbon (3.71 Å) is higher than the graphite (3.35 Å), which depicts the expansion of single layer carbon content [58]. This single layer carbon content is nothing but the micro graphene sheets of activated carbon that is roughly parallel, quite defective and non-planar according to the "falling cards" model proposed by Dahn et al. [59]. In order to measure the single layer carbon sheets, the R-value was calculated based on the formula as reported in ref. [59]. Normally, the R-factor is obtained from the ratio between the height of (002) Bragg's peak and to the background. The calculated R-factor values are 2.2, 2.0 and 1.9 corresponding to the J-600, J-700 and J-800, respectively. The decreasing R-factor with increasing activation temperature infers the expansion of single layer carbon content due to chemical activation [60,61]. During KOH activation, the aligned structural domains in the carbon matrix are getting broken due to the intercalation of the potassium compounds [61]. Therefore, the obtained lesser R-value at high activation temperature (800 °C) infers that the graphene sheets are randomly distributed as single layers with a lesser degree of graphitization and edge orientation [60]. In other words, the lesser degree of graphitization confirms the lacking of long-range three-dimensional order in the micrographene sheets of activated carbon.

To further validate the nature of prepared porous carbons, Raman analysis was carried out, and the respective spectra are provided in Fig. 4b. The prepared porous carbons exhibit the two most prominent features of amorphous materials, namely, D-band appearing at ~1350 cm^{-1} and the G-band at ~1600 cm^{-1}. In addition, one could clearly observe insignificant broadband around 2700–3000 cm^{-1} that corresponds to the unresolved 2D band at ~2700 cm^{-1} and G + D band at ~2930 cm^{-1} [62]. The D band, which is known as the disorder or defect band originates due to the presence of irregularities in the carbon structure and is ascribed to the out-of-plane vibrations from A1g modes whereas the G band is ascribed to in-plane vibrations from E2g modes. The intensity of a D-band is considered to be directly proportional to the extent of defects in the sample. The 2D band is the second order of D band that results from a two-phonon lattice vibrational process, but unlike the D band, it is not activated by the vicinity to defects [63]. But, the G + D band, which is associated with the combination mode of D and G bands, is induced by disorders of the carbon structure [64]. This sort of Raman spectra with second order bands (2D and G + D) corroborates the presence of onion-like nanostructures (OLNs) [62,65–67]. Moreover, the I_D/I_G ratio obtained with the relative intensities of D and G bands is widely used for characterizing the defect quantity of graphitic material. The calculated I_D/I_G ratios are in between 0.92 and 0.98, which indicates the highly disordered amorphous nature of the carbon [68]. It can be seen that the I_D/I_G ratio increases with increasing activation temperature that infers the low graphitization degree of carbon at higher activation temperature. Since KOH activation favours less graphitic carbon, the highly graphitic layers are left un-activated and less dominant. Therefore, these layers rearrange disorderly leading to a lower degree of graphitization at higher activation temperatures [69].

The surface composition of the prepared carbon is characterized using the FTIR spectroscopic analysis, and the resultant FTIR spectra of the prepared porous carbons are shown in Fig. 4c. All the three porous carbons exhibit similar spectral features with three important functional groups, including the –OH, C═O, and C–O, respectively. The –OH stretching observed around 3448 cm^{-1} is mainly attributed to the chemisorbed water molecules and hydroxyl groups on carbon. The peaks around ~1585 cm^{-1} and ~1035 cm^{-1} are derived from the C═O and C–O stretching vibrations, respectively and the peak at ~496 cm^{-1} is attributed to the C–C stretching vibrations [70]. In general, the activated carbon samples show only a few functional groups with reduced intensities since the functional groups get reduced during the activation process [71,72].

The elemental analysis and surface chemistry of the prepared porous carbons are further studied using XPS, and the obtained results are shown in Fig. 5 and Table 2. The XPS survey scans of porous carbons provided in Fig. 5a shows two prominent peaks for the existence of carbon (C 1s) and oxygen (O 1s) at binding energies of 284.1 and 531.7 eV, respectively. The selective existence of C 1s and O 1s peaks elucidated the purity of prepared porous carbons. The C 1s core level spectrum (Fig. 5b) of all the porous carbons are deconvoluted into three significant peaks where the one prominent peak with dominant

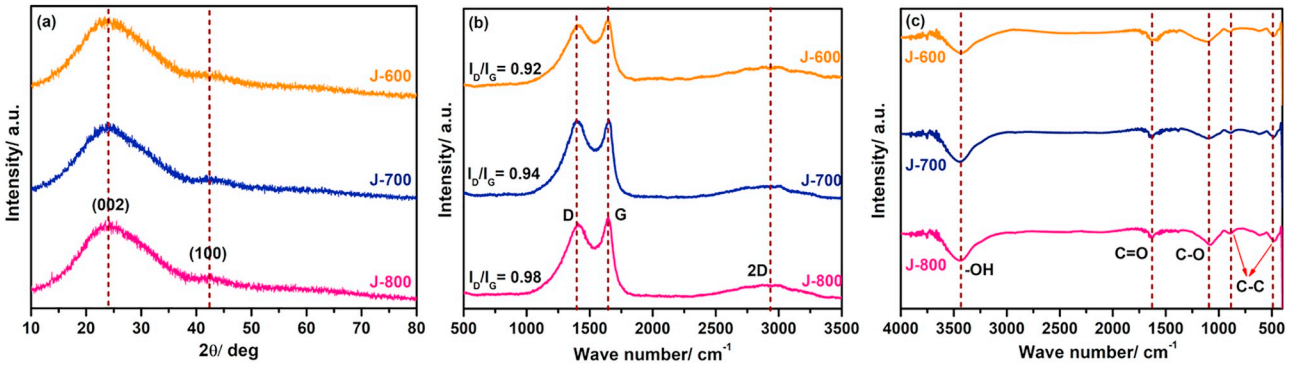

Fig. 4. (a) XRD patterns, (b) Raman spectra, and (c) FTIR spectra of prepared porous carbons.

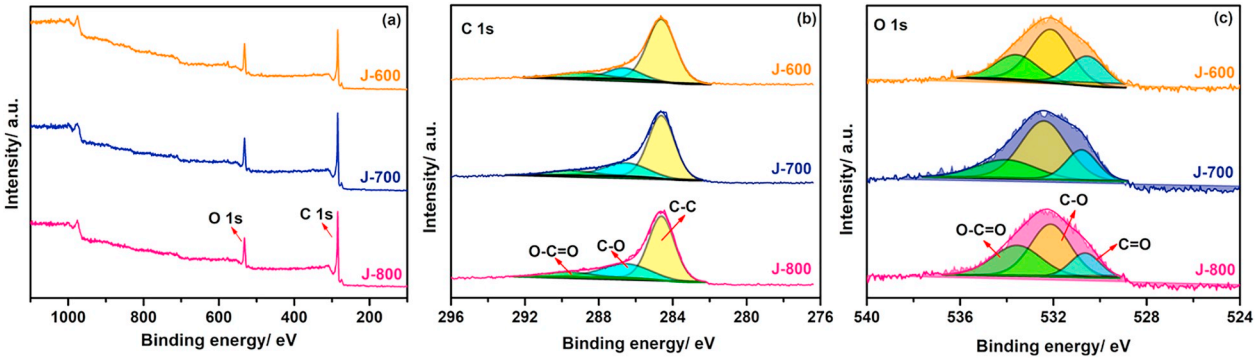

Fig. 5. XPS spectra of prepared porous carbons: (a) survey scan; high-resolution scans for (b) carbon C 1s, and (c) oxygen O 1s.

Table 2
XPS elemental analysis of prepared porous carbons.

Porous carbons	C 1s (at.%)	O 1s (at.%)	N 1s (at.%)	O/C ratio	N/C ratio
J–600	80.23	18.37	1.40	0.23	0.017
J–700	83.10	15.58	1.32	0.19	0.016
J–800	84.02	14.7	1.28	0.16	0.015

intensity at a binding energy of 284.8 eV corresponds to the sp^3 hybridized carbon component, C—C. Whereas the other two peaks at binding energies of 286.5 and 289.0 eV were assigned to the oxide components, C—O and O–C = O respectively [57]. Similarly, in Fig. 5c, the deconvolution of O 1s core level spectra also results in three peaks at binding energies of 530.7, 532.1, and 533.6 eV that can be assigned to the C=O, C—O, and O–C = O respectively [38]. Thus, the XPS analysis infers the presence of oxygen functional groups, which increases the wettability of the electrode and also increases the specific capacitance by involving in redox reactions contributing to pseudocapacitance [73].

The prepared porous carbons consist of almost 80–85 at.% of carbon with 15–18 at.% of oxygen and the remaining amount of nitrogen (Table 2). However, this sensible presence of nitrogen and oxygen moieties enhances the electrochemical properties of the prepared porous carbons. Here, the carbon content increases with increasing carbonization temperature, whereas the oxygen and nitrogen content decreases. The O/C ratio decreases with the increasing activation temperature, which might be due to the decarboxylation reactions that result in the carbon-rich products at higher activation temperature [74]. Furthermore, the loss of nitrogen content from 1.40 at.% (J–600) to 1.28 at.% (J–800) on increasing activation temperature is due to the formation and emission of gaseous nitrogen-containing compounds at high temperatures [75]. The loss of nitrogen atoms with KOH activation, especially at a higher temperature (800 °C) is evident as per previous reports [69]. In conclusion, the O/C and N/C ratios decrease with increasing activation temperature and provide a carbon-rich product as obtained with J–800.

3.3. Electrochemical properties of porous carbon electrodes (three electrode system)

The electrochemical impedance spectroscopy is a potential tool for investigating the ion transport kinetics at the electrode-electrolyte interface. The impedance analysis is carried out for the prepared porous carbon electrodes at an open circuit potential in the frequency range of 1 Hz to 0.1 MHz, and the corresponding Nyquist plot is given in Fig. 6a. In general, the equivalent series resistance includes electrolyte resistance (R_s), interfacial resistance (R_{ct}), and ion diffusion resistance that corresponds to the x-axis intercept at high frequency, semi-circle at mid-frequency and a vertical line at a low frequency of Nyquist plot, respectively. The Nyquist plots of the electrodes display a semicircle obtained at the high-frequency region, demonstrating the charge-transfer resistance followed by a straight line sloping at the low-frequency region inferring the ion diffusion within the electrode [76]. The obtained R_s values are 0.58, 0.57, and 0.55 Ω for J–600, J–700, and J–800 electrodes, respectively. Similarly, the charge transfer resistances, R_{ct} are found to be 1.75 for J–600, 0.95 for J–700 and 1.05 Ω for J–800. The smaller semicircle and nearly vertical line of J–800 clearly portrays the smaller solution resistance (0.55 Ω), charge transfer resistance (1.05 Ω) and faster ion transfer kinetics of the electrode material. Further, the relatively shorter length of a straight line at low frequency further validates the faster ion transfer from the electrolyte solution into the hierarchical pores of carbon electrode [57].

To further substantiate the obtained impedance results, the admittance characteristics of the electrodes are obtained and provided in Fig. 6b. The admittance plot is generally characterized using the Knee frequency, which is defined as the maximum frequency at which the resistance behaviour becomes negligible, and the capacitive behaviour becomes dominant [77]. The observed high Knee frequency of 316.31 Hz further validates the low charge transfer resistance of the J-800 electrode [77]. Even though J–700 exhibits much higher Knee frequency, i.e., lower charge transfer resistance, the ion transfer kinetics is very poor. Moreover, the variation of phase angle with frequency is provided in Fig. 6c. The phase angles are observed around 60°, which infers the contribution of partial ideal capacitive behaviour or redox nature of the porous carbons due to the existence of oxygen-containing functional groups [78]. Thus, the observed lower phase angles substantiate the quick ionic diffusion of the prepared electrodes. In addition, the relaxation time is calculated from the frequency values at a phase angle −45° using equation, Eq. (6) [79],

$$\tau = \frac{1}{2\pi f} \tag{6}$$

The obtained τ values are 16, 47 and 64 ms (milliseconds) for J–600, J-700, and J-800, respectively. The higher relaxation time of J–800 (64 ms) validates the prolonged discharging process of the electrode, which in turn can deliver energy for an extended time [77]. Fig. 6d shows the Nyquist plot of J–800 electrode at various applied potentials (0 to 0.8 V). This obtained trend of Nyquist plot with varying applied voltages validates the capacitive behaviour and ionic diffusion in the electrode structure [80]. The change in behaviour observed at an applied voltage of 0.8 V validates with the onset of oxygen evolution observed during CV scans at the same potential. Therefore, from the detailed impedance analysis, the J–800 is observed to possess better conductivity with lesser solution resistance (0.55 Ω), charge transfer resistance (1.05 Ω), high Knee frequency (316.31 Hz), higher relaxation time (64 ms), and enhanced ionic diffusion.

Further, the cyclic voltammetry analyses were carried out for the prepared porous carbon electrodes at a scan rate of 5 mV s^{-1} over the potential range of 0 to 0.8 V vs. Ag/AgCl in 0.5 M H_2SO_4 electrolyte and are given Fig. 7a. It can be seen that all the electrodes display a quasi-

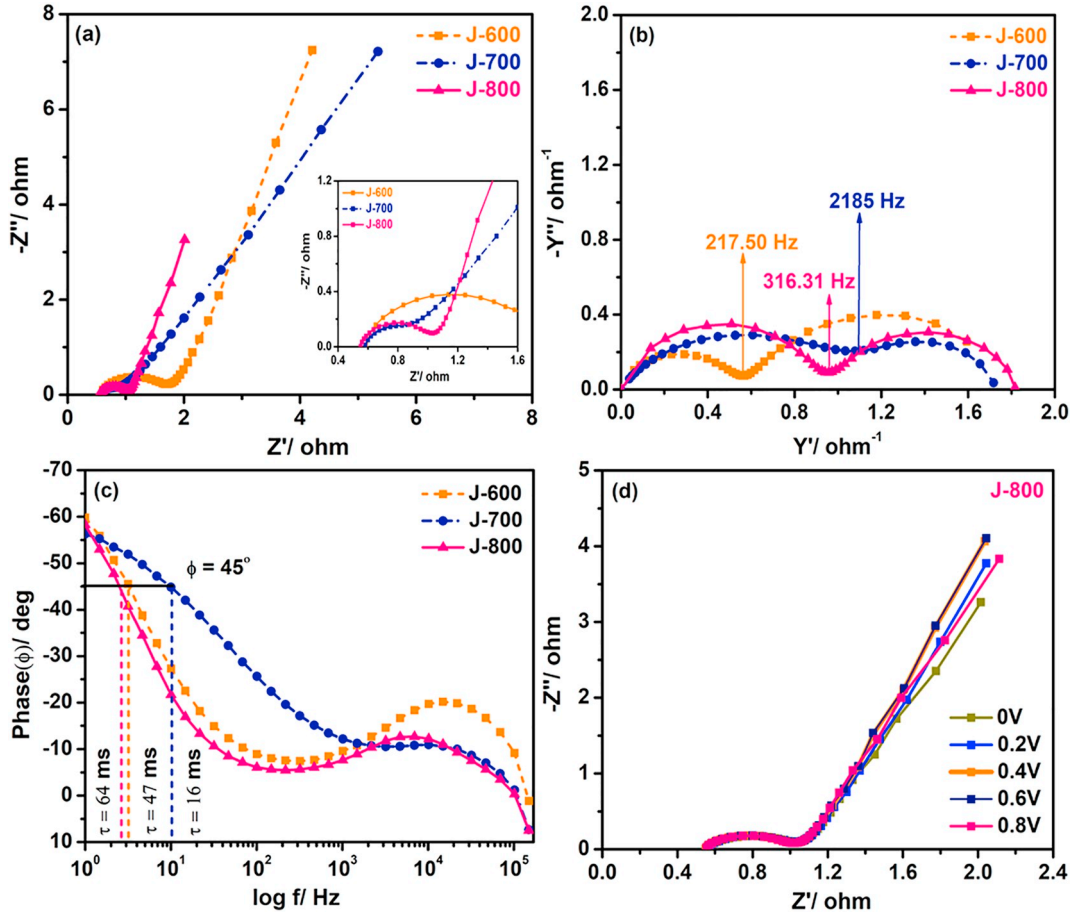

Fig. 6. (a) Nyquist plot, (b) admittance plot, and (c) log f vs. phase plot of prepared porous carbons, and (d) Nyquist plot of J–800 at various applied voltages.

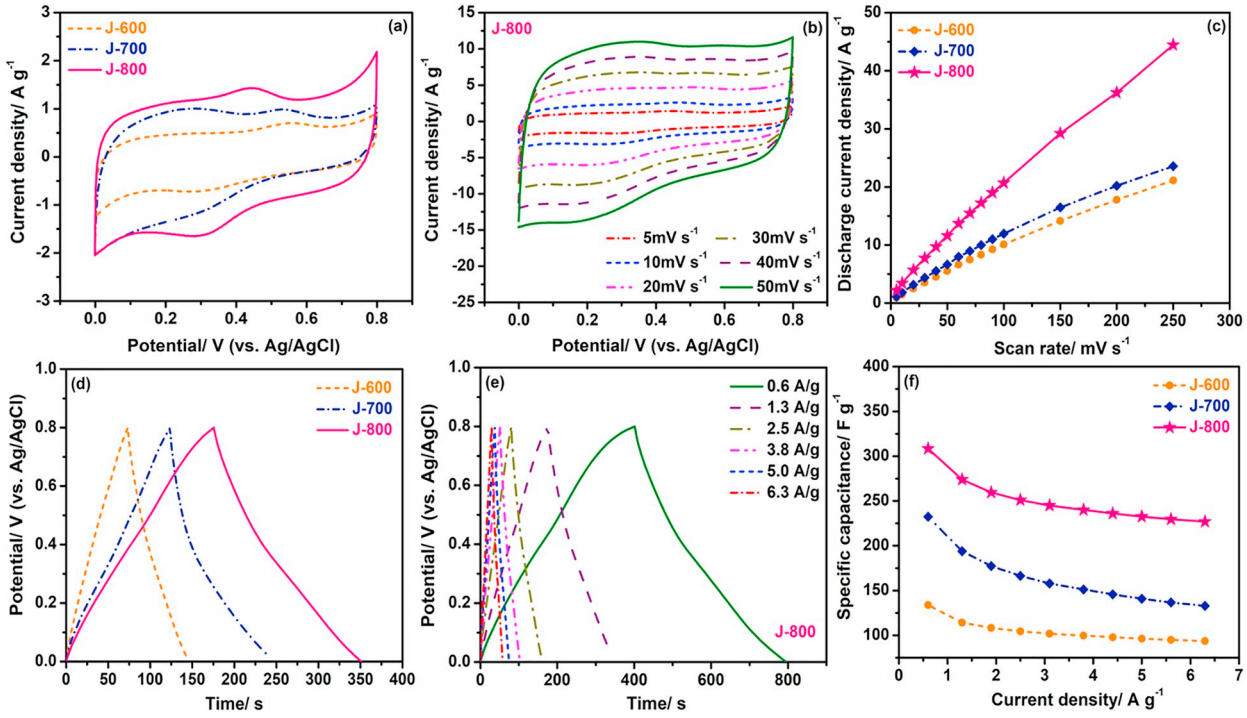

Fig. 7. (a) Comparative CV curves of porous carbons at a scan rate of 5 mV s^{-1}, (b) CV curves of J–800 at various scan rates, (c) scan rate vs. discharge current plot of porous carbons, (d) comparative GCD curves of porous carbons at a current density of 1.3 A g^{-1}, (e) GCD curves of J–800 at various current densities, and (f) specific capacitance vs. current density plot of porous carbons.

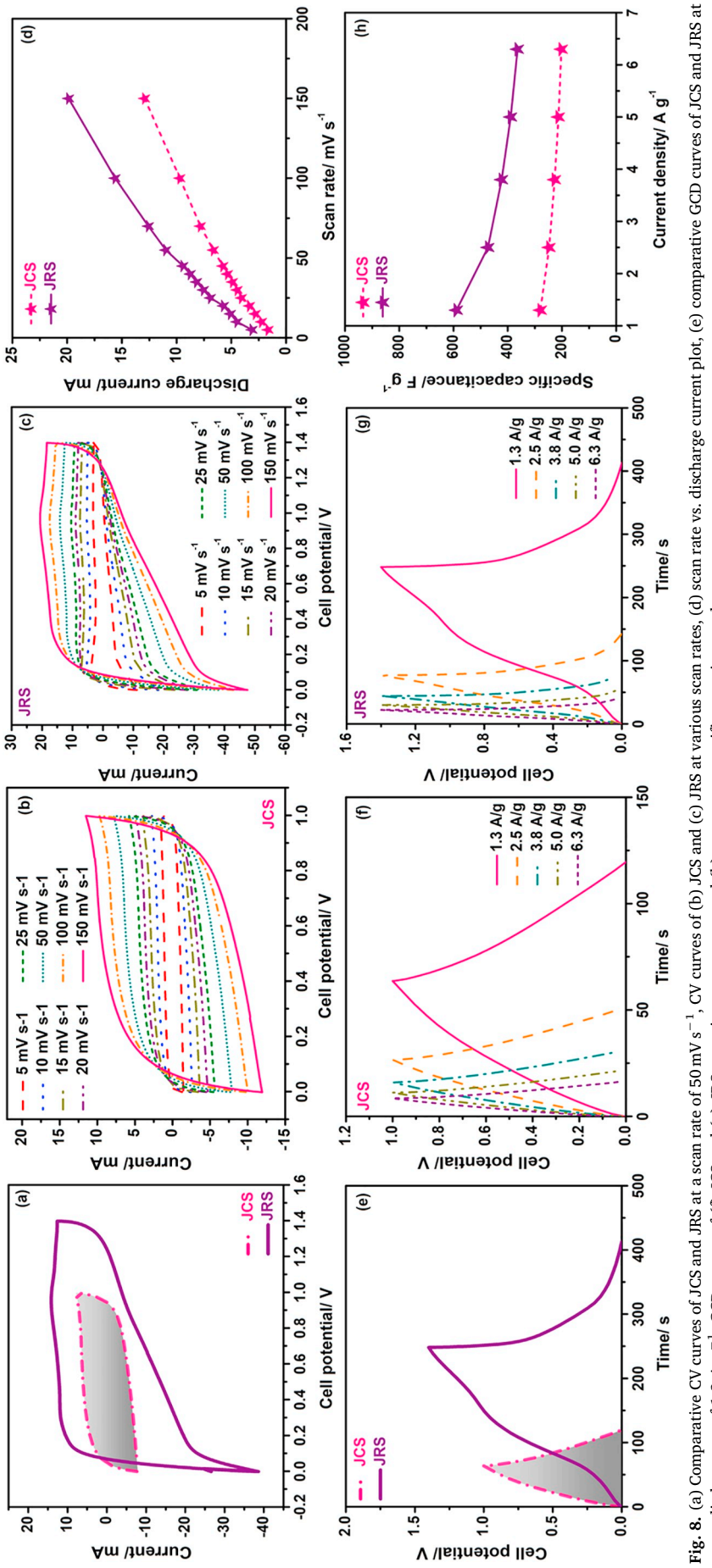

Fig. 8. (a) Comparative CV curves of JCS and JRS at a scan rate of 50 mV s^{-1}, CV curves of (b) JCS and (c) JRS at various scan rates, (d) scan rate vs. discharge current plot, (e) comparative GCD curves of JCS and JRS at an applied current of 1.3 A g^{-1}, GCD curves of (f) JCS and (g) JRS at various scan rates, and (h) current vs. specific capacitance plot.

rectangular behaviour with the existence of a broad hump inferring the combination of both EDLC and pseudocapacitive behaviour. The presence of hump contributing the pseudocapacitance was mainly caused by the reversible redox reactions of the oxygen-containing functional groups present in the samples [49]. Among the prepared porous carbons, J–800 covers a maximum current area and provides a maximum specific capacitance of 477 F g^{-1} than the J–700 (340 F g^{-1}) and J–600 (250 F g^{-1}) electrodes. The representative cyclic voltammogram of J-800 electrode at different scan rates from 5 to 50 mV s^{-1} are shown in Fig. 7b. Interestingly, the quasi-rectangular nature of the CV curves remain unchanged even at a high scan rate of 50 mV s^{-1} and it delivers a higher current with increasing scan rates validating the unintermittent accessibility of electrolyte ions, low internal resistance, better rate capability and faster kinetics for the electric double layer formation due to the hierarchically porous nature of J–800. To further understand the diffusion progress of electrolyte ions with increasing scan rates, the scan rate versus discharge current plot up to 250 mV s^{-1} is provided for all the electrodes in Fig. 7c. The calculated mean areal capacitance is 0.04, 0.05 and 0.10 F cm^{-2} for J–600, J-700 and J-800, respectively. Thus, J–800 has displayed a better linear current behaviour and has provided a maximum mean areal capacitance of 0.10 F cm^{-2}, which demonstrated the better accessibility of electrolyte ions even at higher scan rates of 250 mV s^{-1}.

The galvanostatic charge-discharge analysis was carried out to further investigate the capacitive charge storage behaviour of the prepared porous carbon electrodes. Fig. 7d shows the comparative GCD curve of all the electrodes at a current density of 1.3 A g^{-1}. The GCD curves are not exactly triangular and are slightly distorted, exhibiting the characteristics of both EDLC and pseudocapacitive behaviour. The pseudocapacitive behaviour is attributed to the presence of electroactive oxygen functional groups in the electrodes, as explained earlier [49]. Among these, J–800 shows a better capacitive behaviour with a calculated specific capacitance of 274 F g^{-1} which is significantly higher than that of J–600 (114 F g^{-1}) and J–700 (194 F g^{-1}). Moreover, J–800 has provided more than twice of the specific capacitance of J–600. Hence, the GCD analysis was carried out at various current densities from 0.6 A g^{-1} to 6.3 A g^{-1} for J–800 and is provided in Fig. 7e. Further, the calculated specific capacitances are plotted with respect to the applied current densities to understand the rate capability of the electrodes (Fig. 7f). The obtained specific capacitance of J–800 (308 F g^{-1}) at 0.6 A g^{-1} has a sensible decrement (227 F g^{-1}) even at a higher current density of 6.3 A g^{-1}. Thus J–800 has retained almost 74% of its initial capacitance even at high current density whereas J–700 and J–600 has retained only 69% and 57%, respectively. The retarding specific capacitance with increasing current densities is quite common since at lower current densities, the electrolyte ions diffuse into the electrode and access the inner space of the material whereas at higher current densities the ionic motion in and out of the pores is much faster and hence the electrolyte ions cannot completely access the electrode material. But, the J–800 electrodes has retained almost its initial specific capacitance at higher current densities than the prepared other electrodes.

This significant electrochemical performance of J–800 with a maximum specific capacitance of 477 F g^{-1} at 5 mV s^{-1} and 274 F g^{-1} at 1.3 A g^{-1} is obviously due to the (i) high BET specific surface area, (ii) hierarchical porous network of micro and mesopores, (iii) high microporous surface area, (iv) maximum pore volume, (iv) unique carbon onion–like morphology, and (v) existence of oxygen-containing functional groups. The above mentioned morphological and textural features of J–800 electrodes with the prosperous count of micropores and macropores have regulated the supply and storage of electrolyte ions/charges. Because, the small mesopores can play adsorption and transporting role, whereas, the micropores are liable for penetration of electrolyte ions and faster charge accommodation. The abundant interconnected micro/mesopores would provide low-resistant pathways and played an essential role to make the shorter distance for ions through the porous particles. In addition, the interconnected pores structure can also provide good charge propagation ability for high scan rates/current densities. Moreover, the unique morphology and porous nature of J-800 electrode provide better conductivity with lesser solution resistance (0.55 Ω), charge transfer resistance (1.05 Ω), high Knee frequency (316.31 Hz), higher relaxation time (64 ms), and enhanced ionic diffusion.

3.4. Electrochemical properties of fabricated supercapacitors (two electrode system)

Based on the remarkable electrochemical performance of the J–800 electrodes, the symmetric supercapacitor (J–800 ‖ J–800) was fabricated. Further, the redox-mediated electrochemical performance of the device was studied in 0.5 M H_2SO_4 + 0.005 M KI electrolyte in comparison with conventional 0.5 M H_2SO_4 electrolyte. Various concentrations of KI were used, and the best composition (0.005 M) was identified to obtain better electrochemical performance. The supercapacitor studied using a conventional (J–800 | H_2SO_4 | J–800), and redox additive (J–800 | H_2SO_4–KI | J–800) electrolytes are named as JCS and JRS, respectively, hereafter. Fig. 8a shows the comparative CV curves of fabricated supercapacitors JCS and JRS at a scan rate of 50 mV s^{-1}. It can be seen that the JCS shows an ideal rectangular shape that deliberates the typical electric double-layer based capacitive behaviour whereas the JRS has reflected an increased current area with a non-ideal capacitive behaviour due to the redox reactions of KI. Further, the JRS has delivered an operating cell voltage of 1.4 V, which is evidently comprehensive than JCS (1 V). The significantly larger current area delivered by JRS is obviously attributed to the incorporation of redox-additive electrolytes with the iodide based redox pairs including $3I/I_3$, $2I/I_2$, $2I_3/3I_2$ and I_2/IO_3 [42–44]. The improved electrochemical performance is explicitly due to better surface charge storage ability of the porous carbon electrode with the aid of redox pairs as proposed by Chen et al. [34]. According to his mechanism, the interface reactions take place at both the internal and external surface of the porous-structured electrodes, as given below. Initially, (i) the iodide redox species ($R_{(bulk)}/O_{(bulk)}$) such as I, I_2, I_3 and IO_3 undergoes solvation or de-solvation process for matching the pore size of the electrode. (ii) After the solvation/de-solvation process, the resultant redox species ($R_{(pore)}/O_{(pore)}$) with appropriate ionic sizes access the maximum number of pores, (iii) Further, the $R_{(pore)}/O_{(pore)}$ reaches the transition state (R^*/O^*) to facilitate the electron transfer. (iv) Subsequently, the highly favourable micropores and mesopores promote the adsorption process resulting in the formation of $R_{(ads)}/O_{(ads)}$. Finally, the electron transfer takes place, and the transformation of adsorbed redox species occurs based on the following redox reactions (Eqs. (7)–(10)).

$$3I^- \leftrightarrow I_3^- + 2e^- \quad (7)$$

$$2I^- \leftrightarrow I_2 + 2e^- \quad (8)$$

$$2I_3^- \leftrightarrow 3I_2 + 2e^- \quad (9)$$

$$I_2 + 6H_2O \leftrightarrow 2IO_3^- + 12H^+ + 10e^- \quad (10)$$

These redox reactions takes place between the iodide redox pairs at the positive electrode and contribute pseudocapacitance [46] whereas; the K^+ ions of redox additive electrolyte undergo electrosorption on the negative electrode and contribute electric double layer capacitance. Further, the cyclic voltammetry was carried out at various scan rates ranging from 10 to 150 mV s^{-1} for both the supercapacitors, JCS and JRS (Fig. 8b & c). The rectangular shape of JCS remains unchanged even at a higher scan rate of 150 mV s^{-1} that infers the ideal capacitive behaviour of the fabricated EDLC (Fig. 8b). As shown in Fig. 8c, the increasing current area with increasing scan rates and prominence of redox peaks without peak shifting even at higher scan rates infers the better electrochemical reversibility of the redox system in JRS. Fig. 8d

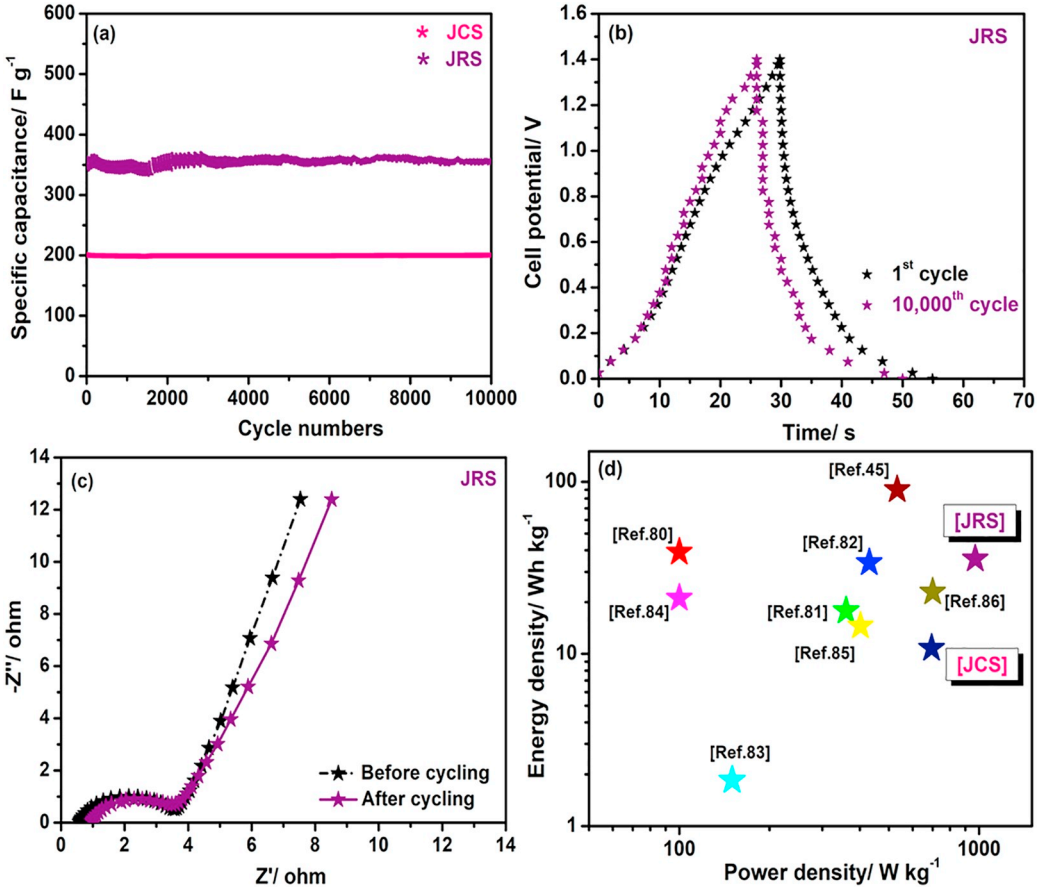

Fig. 9. (a) Cycling stability of the fabricated supercapacitors, (b) comparative GCD curves of JRS at 1st and 10,000th cycle, and (c) Ragone plot of fabricated devices.

shows the scan rate versus discharge current plot of fabricated supercapacitors. The better linear current behaviour of JRS than JCS even up to a higher scan rate of 150 mV s^{-1} infers the relatively better accessibility of redox-additive electrolyte ions than the conventional one. This further validates that the redox-additive electrolyte with smaller ionic sizes of iodide redox species, i.e., polyiodides such as I^-, I_3^-, I_5^-, and IO_3^- can easily access the micropores and mesopores of the prepared porous J–800 because the ionic sizes of these iodide species ranges around 0.5 to 1.5 nm that is obviously appropriate for accessing the micropores (< 1 nm) and smaller mesopores (< 5 nm) [44].

The galvanostatic charge-discharge characteristics of the fabricated supercapacitors, JCS and JRS, are compared at an applied current of 1.3 A g^{-1} and are provided in Fig. 8e. The JCS deliberates a capacitive behaviour with the incidence of linear, triangle-shaped GCD curve. On the other hand, a faradaic plateau was obtained with JRS, which confirms the occurrence of voltage-dependent redox reactions within the redox system [47]. The GCD curve of JCS reaches a cell voltage of 1 V whereas the JRS provides an extended cell voltage of 1.4 V due to the redox-mediated charge storage mechanism. The GCD curves obtained at various applied currents from 1.3 A g^{-1} to 6.3 A g^{-1} are provided in Fig. 8(f, g). Fig. 8h shows the comparative specific capacitance versus applied current plot of fabricated supercapacitors. The JRS delivers a remarkably higher specific capacitance of 589 F g^{-1} than JCS (280 F g^{-1}) at an applied current of 1.3 A g^{-1}. Even at a high current of 6.3 A g^{-1}, the JRS provides a maximum specific capacitance of 364 F g^{-1} than the JCS (202 F g^{-1}). Thus, a nearly three times enhanced specific capacitance is obtained with the redox-additive mediated storage mechanism of JRS than the conventional EDLC storage of JCS with pristine electrolyte. This enhanced electrochemical performance of JRS is highly contributed to the pseudocapacitive behaviour delivered by the iodide redox species present in the redox additive electrolyte. Thus, the iodide ions play a dual role by delivering good ionic conductivity and a favourable pseudocapacitive effect on the fabricated supercapacitor, JRS. It is clear that the unique hierarchical porous network of prepared J–800 with the co-existence of both micro and mesopores seems to be the most appropriate electrode texture for both the electrosorption and the faradaic reactions related to the polyiodide electron transfers involved during the charging process.

Stability is always a mandatory performance-analysing parameter when it comes to the practical application of the fabricated devices. Hence, the stability of the supercapacitors, JCS and JRS was carried out at a high current of 6.3 A g^{-1} for about 10,000 cycles and is provided in Fig. 9a. JRS has provided an initial specific capacitance of (364 F g^{-1}) and ended up with 352 F g^{-1} at 10,000th cycle and retained almost 96% of its initial capacitance. Similarly, JCS has also retained almost 96% of its initial capacitance since, the hierarchical porous structure and unique carbon onion–like morphology of J–800 electrodes provide a low-resistant pathway and good charge propagation ability to the fabricated device. Thus without losing the stability, an enhanced specific capacitance is attained with the redox additive based aqueous electrolyte. In order to provide a clear picture of the stability, the comparative GCD curves of JRS at 1st and 10,000th cycle is provided in Fig. 9b. The galvanostatic charge-discharge behaviour of JRS remains unchanged even after 10,000 cycles and has displayed a merely slight change with charging and discharging period which results in a relative loss (4%) of specific capacitance than initial specific capacitance.

The EIS spectra of JRS before and after cycling stability are provided in Fig. 9c. After 10,000 cycles, the solution resistance has slightly increased from 0.6 Ω to 0.9 Ω, whereas there is no significant change in the charge transfer resistance validating the 96% retention of initial specific capacitance by JRS. Moreover, the negligible change in resistance of JRS even after 10,000 cycles, infers that the existence of

Table 3
Comparison of specific capacitance and energy density with related recent reports.

Electrode	Redox additive	Supporting electrolyte	Specific capacitance ($F g^{-1}$)	Condition ($A g^{-1}$)	Energy density ($Wh kg^{-1}$)	Power density ($W kg^{-1}$)	Cycles	Ref
AC (Commercial: Loba Chemie)	KI	H_2SO_4	1072	2.1	20.49	–	5000	[45]
Carbon naosheet (MOF derived)	KI	H_2SO_4	49	2	90	533	5000	[47]
AC (mango kernel)	p-Hydroxyproline	H_2SO_4	587.1	1	34.3	–	5000	
AC (Commercial: Loba Chemie)			208.8	1	13.4	–	–	[81]
AC (felt)	$K_3[Fe(CN)_6]$ 2,6-(DHAQ)	KOH	79	2 mV s^{-1}	39.1	100	5000	[82]
AC (corn silk)	Alizarin Bromoamine	H_2SO_4	260.8	0.5	17.8	360	1000	[83]
Porous carbon (MgO template)	$FeBr_3$	H_2SO_4	885	2	33.9	430	10,000	[84]
AC (charcoal)	Hydroquinone *p*-Phenylenediamine	H_2SO_4	116.23	2	1.85	150	2000	[85]
Porous carbon (ZnO template)	Phosphotungstic acid Potassium ferricyanide	H_2SO_4	77	2	21.1	100	5000	[86]
N,P doped carbon microsphere/rGo nanocomposite	KI	H_2SO_4	654	2	14.53	402	4000	[87]
PANI/CNT	Fe^{3+}/Fe^{2+}	H_2SO_4 - PVA	1547	2	22.9	700	2000	[88]
Porous carbon (*P. juliflora* pods)	–	H_2SO_4	279	1.3	10.8	694	10,000	Present work
	KI	H_2SO_4	589		35.7	971		

hierarchical porous network with unique onion–like morphology serves a better charge transfer pathway for polyiodides during the charging process. Finally, based on the GCD curves the energy density and power density of fabricated supercapacitors are calculated, and the respective Ragone plot along with the energy and power density of other related recent reports are also provided for comparison in Fig. 9d. Further, the detailed comparison of those reports with the present work is tabulated (Table. 3) [81–88]. It is obviously clear from the Ragone plot that the EDLC with redox additive electrolyte has provided an enhanced energy density than the EDLC without redox additive. The JRS has provided a remarkable energy density of 35.7 Wh kg^{-1} at an enhanced power density of 971 W kg^{-1}. On the other hand, JCS delivered an energy density of 10.8 Wh kg^{-1} at a power density of 694 W kg^{-1}. Thus, the incorporation of redox additive based aqueous electrolyte has enhanced the energy density without sacrificing the power density and stability of conventional EDLC.

Overall, it is evident that the present work appears to be novel management and control technologies to eradicate the environmentally benign weed by adapting it as a renewable raw material for energy application. The porous carbon obtained from the pods of *P. juliflora* is significantly endowed with the following salient features that turn it into a novel electrode material for the supercapacitors, i) the highly disordered amorphous nature, ii) surface enriched oxygen functional groups contributing pseudocapacitance, iii) a unique onion like nanostructure with high BET specific surface area of 967 $m^2 g^{-1}$, iii) existence of both micro and mesopores which aids the charge storage and facilitates the transfer kinetics, and vi) enhanced conductivity that favours faster charge transfer kinetics. Further, the optimal utilization of KI redox additive leads to the formation of carbon/iodide interface resulting in an exceptional electrochemical behaviour. Hence, the fabricated JRS supercapacitor provides an enhanced energy density of 35.7 Wh kg^{-1} at an improved power density 971 W kg^{-1} with remarkable stability over 10,000 cycles. Thus, the present work divulges the usage of eco-waste, the *P. juliflora* pods for the production of porous carbon and electrode material for the redox additive mediated supercapacitor application.

4. Conclusion

The knack of reforming the most threatening, invasive weed into an efficient electrode material for the application of supercapacitor is achieved with the present work. The enhanced performance of the device is carefully investigated with the detailed characterization of prepared electrode materials. The R-factor and I_D/I_G ratios calculated from XRD and Raman analysis, substantiate the existence of structural defects on KOH activation. The effect of activation temperature on the morphology and pore formation is discussed in detail. The morphological characteristics were investigated with FESEM and TEM analysis and the unique onion–like morphology was observed to be the origin for the enhanced electrochemical performance of the prepared *P. juliflora* carbon. Moreover, the BET analysis reports the high specific surface area (967 $m^2 g^{-1}$) and exclusively hierarchical porous network of prepared J–800 electrode material. Impedance analysis elucidates the better conductivity of J–800 with lesser solution resistance (0.55 Ω), charge transfer resistance (1.05 Ω), high Knee frequency (316.31 Hz), higher relaxation time (64 ms), and enhanced ionic diffusion rate. Thus, J–800 has exhibited a sensible specific capacitance of 274 F g^{-1} at a current density of 1.3 A g^{-1} based on which a symmetric EDLC was fabricated out of J–800 to provide an energy density of 10.8 Wh kg^{-1} at a power density of 694 W kg^{-1} in H_2SO_4. Further, the performance of the prepared EDLC is enhanced to achieve a remarkable energy density of 35.7 Wh kg^{-1} at a power density of 971 W kg^{-1} by employing the redox additive based aqueous electrolyte. Moreover, the redox-mediated supercapacitor has also demonstrated excellent cycling stability for about 10,000 cycles with almost 96% capacitance retention. Thus, the aim of enhancing the energy density without sacrificing the power density and cycling stability provided by the conventional electrolyte is achieved with the redox-additive based aqueous electrolyte. Moreover, an environmental threat derived low-cost biomass is employed as an electrode material for the most trending energy application.

Acknowledgement

The lead authors (S.S) would like to thank DST-PURSE program, Bharathiar University, for providing financial support. Prof. Yun Sung Lee acknowledges the Ministry of Science, ICT and Future Planning of South Korea for providing a National Research Foundation of Korea (NRF) grant (No. 2019R1A4A2001527).

References

[1] P. Simon, Y. Gogotsi, B. Dunn, Materials science. Where do batteries end and supercapacitors begin? Science 343 (2014) 1210–1211.
[2] F. Beguin, E. Frackowiak (Eds.), Supercapacitors: Materials, Systems and Applications, Wiley-VCH, Weinheim, 2013.
[3] B.E. Conway, Electrochemical Supercapacitors: Scientific Fundamentals and Technological Applications, Springer, 1999.
[4] P. Simon, A. Burke, Nanostructured carbons: double-layer capacitance and more, Electrochem. Soc. Interface 17 (2008) 38–43.
[5] P. Simon, Y. Gogotsi, Capacitive energy storage in nanostructured carbon–electrolyte systems, Acc. Chem. Res. 46 (2013) 1094–1103.
[6] B. Yao, L. Yuan, X. Xiao, J. Zhang, Y. Qi, J. Zhou, J. Zhou, B. Hu, W. Chen, Paper-based solid-state supercapacitors with pencil-drawing graphite/polyaniline networks hybrid electrodes, Nano Energy 2 (2013) 1071–1078.
[7] Z. Chen, J. Wen, C. Yan, L. Rice, H. Sohn, M. Shen, M. Cai, B. Dunn, Y. Lu, High-performance supercapacitors based on hierarchically porous graphite particles, Adv. Energy Mater. 1 (2011) 551–556.
[8] Y. Wang, Z. Shi, Y. Huang, Y. Ma, C. Wang, M. Chen, Y. Chen, Supercapacitor devices based on graphene materials, J. Phys. Chem. C 113 (2009) 13103–13107.
[9] W.K. Chee, H.N. Lim, Z. Zainal, N.M. Huang, I. Harrison, Y. Andou, Flexible graphene-based supercapacitors: a review, J. Phys. Chem. C 120 (2016) 4153–4172.
[10] D. Chen, L. Yang, J. Li, Q. Wu, Effect of self-doped heteroatoms in biomass-derived activated carbon for supercapacitor applications, ChemistrySelect 4 (2019) 1586–1595.
[11] D.J. Ahirrao, S. Tambat, A.B. Pandit, N. Jha, Sweet-lime-peels-derived activated-carbon-based electrode for highly efficient supercapacitor and flow-through water desalination, Chemistry Select 4 (2019) 2610–2625.
[12] K.H. An, W.S. Kim, Y.S. Park, J.M. Moon, D.J. Bae, S.C. Lim, Y.S. Lee, Y.H. Lee, Electrochemical properties of high-power supercapacitors using single-walled carbon nanotube electrodes, Adv. Funct. Mater. 11 (2001) 387–392.
[13] A.I. Najafabadi, S. Yasuda, K. Kobashi, T. Yamada, D.N. Futaba, H. Hatori, M. Yumura, S. Iijima, K. Hata, Extracting the full potential of single-walled carbon nanotubes as durable supercapacitor electrodes operable at 4 V with high power and energy density, Adv. Mater. 22 (2010) E235–E241.
[14] L.-F. Chen, X.-D. Zhang, H.-W. Liang, M. Kong, Q.-F. Guan, P. Chen, Z.-Y. Wu, S.-H. Yu, Synthesis of nitrogen-doped porous carbon nanofibers as an efficient electrode material for supercapacitors, ACS Nano 6 (2012) 7092–7102.
[15] X. Yan, Z. Tai, J. Chen, Q. Xue, Fabrication of carbon nanofiber-polyaniline composite flexible paper for supercapacitor, Nanoscale 3 (2011) 212–216.
[16] M. Zhang, M. Chen, N. Reddeppa, D. Xu, Q. Jing, R. Zha, Nitrogen self-doped carbon aerogels derived from trifunctional benzoxazine monomers as ultralight supercapacitor electrodes, Nanoscale 10 (2018) 6549–6557.
[17] Y. Zhang, C. Zhao, W.K. Ong, X. Lu, Ultrafast-freezing-assisted mild preparation of biomass-derived, hierarchically porous, activated carbon aerogels for high-performance supercapacitors, ACS Sustain. Chem. Eng. 7 (2019) 403–411.
[18] M. Rose, Y. Korenblit, E. Kockrick, L. Borchardt, M. Oschatz, S. Kaskel, G. Yushin, Hierarchical micro and mesoporous carbide-derived carbon as a high-performance electrode material in supercapacitors, Small 7 (2011) 1108–1117.
[19] J. Eskusson, A. Janes, A. Kikas, L. Matisen, E. Lust, Physical and electrochemical characteristics of supercapacitors based on carbide derived carbon electrodes in aqueous electrolyte, J. Power Sources 196 (2011) 4109–4116.
[20] L. Miao, D. Zhu, M. Liu, H. Duan, Z. Wang, Y. Lv, W. Xiong, Q. Zhu, L. Li, X. Chai, L. Gan, N, S co-doped hierarchical porous carbon rods derived from protic salt: facile synthesis for high energy density supercapacitors, Electrochim. Acta 274 (2018) 378–388.
[21] L. Miao, X. Qian, D. Zhu, T. Chen, G. Ping, Y. Lv, W. Xiong, Y. Liu, L. Gan, M. Liu, From interpenetrating polymer networks to hierarchical porous carbons for advanced supercapacitor electrodes, Chinese Chem. Lett. (2019), https://doi.org/10.1016/j.cclet.2019.03.010.
[22] J. Yan, D. Zhu, Y. Lv, W. Xiong, M. Liu, L. Gan, Water-in-salt electrolyte ion-matched N/O codoped porous carbons for high-performance supercapacitors, Chinese Chem. Lett. (2019), https://doi.org/10.1016/j.cclet.2019.05.035.
[23] Z. Song, H. Duan, L. Li, Dazhang. Zhu, T. Cao, Y. Lv, W. Xiong, Z. Wang, M. Liu, L. Gan, High-energy flexible solid-state supercapacitors based on O, N, S-tridoped carbon electrodes and a 3.5 V gel-type electrolyte, Chem. Eng. J. 372 (2019) 1216–1225.
[24] F. Beguin, E. Frackowiak (Eds.), Carbons for Electrochemical Energy Storage and Conversion Systems, CRC Taylor & Francis, 2009.
[25] E. Frackowiak, F. Beguin, Electrochemical storage of energy in carbon nanotubes and nanostructured carbons, Carbon 40 (2002) 1775–1787.
[26] E. Frackowiak, Carbon materials for supercapacitor application, Phys. Chem. Chem. Phys. 9 (2007) 1774–1785.
[27] K. Fic, A. Platek, J. Piwek, E. Frackowiak, Sustainable materials for electrochemical capacitors, Mater. Today 21 (2018) 437–452.
[28] R.T. Shackleton, D.C. Le Maitre, N.M. Pasiecznik, D.M. Richardson, Prosopis: a global assessment of the biogeography, benefits, impacts and management of one of the world's worst woody invasive plant taxa, AoB PLANTS, 2014, p. 6 (plu027).
[29] R.K. Sawal, R. Ratan, S.B.S. Yadav, Mesquite (Prosopis juliflora) pods as a feed resource for livestock -a review, Asian-Australas J Anim Sci. 17 (2004) 719–725.
[30] P. Sennu, H.-J. Choi, S.-G. Baek, V. Aravindan, Y.-S. Lee, Tube-like carbon for Li-ion capacitors derived from the environmentally undesirable plant: Prosopis juliflora, Carbon 98 (2016) 58–66.
[31] P. Sennu, V. Aravindan, M. Ganesan, Y.-G. Lee, Y.-S. Lee, Biomass-derived electrode for next generation lithium-ion capacitors, ChemSusChem 9 (2016) 849–854.
[32] P. Sennu, N. Arun, S. Madhavi, V. Aravindan, Y.-S. Lee, All carbon-based high energy lithium-ion capacitors from biomass: the role of crystallinity, J. Power Sources 414 (2019) 96–102.
[33] J. Yan, Q. Wang, T. Wei, Z.J. Fan, Recent advances in design and fabrication of electrochemical supercapacitors with high energy densities, Adv. Energy Mater. 4 (2013) 1300816.
[34] B. Akinwolemiwa, C. Peng, G.Z. Chen, Redox electrolytes in supercapacitors, J. Electrochem. Soc. 162 (2015) A5054–A5059.
[35] S. Roldan, C. Blanco, M. Granda, R. Menendez, R. Santamar, Towards a further generation of high-energy carbon-based capacitors by using redox-active electrolytes, Angew. Chem. Int. Ed. 50 (2011) 1699–1701.
[36] B. Gorska, E. Frackowiak, F. Beguin, Redox-active electrolytes in carbon/carbon electrochemical capacitors, Curr. Opin. Electrochem. 9 (2018) 95–105.
[37] K. Fic, M. Meller, E. Frackowiak, Interfacial redox phenomena for enhanced aqueous supercapacitors, J. Electrochem. Soc. 162 (2015) A5140–A5147.
[38] B. Akinwolemiwa, G.Z. Chen, Dissolved redox species for the improvement of the performance of supercapacitors, Curr. Top. Electrochem. 19 (2017) 47–65.
[39] E. Frackowiak, K. Fic, M. Meller, G. Lota, Electrochemistry serving people and nature: high-energy eco capacitors based on redox-active electrolytes, ChemSusChem 5 (2012) 1181–1185.
[40] X. Huang, X.N. Sun, X.Y. Chen, Highly-nitrogenated porous carbon for supercapacitor: structure design and redox mechanism of amine/nitro/hydroxyl groups in KOH solution, Int. J. Hydrog. Energy 41 (2016) 18095–18106.
[41] S.T. Senthilkumar, R. Kalai Selvan, J.S. Melo, Redox additive/active electrolytes: a novel approach to enhance the performance of supercapacitors, J. Mater. Chem. A 1 (2013) 12386–12394.
[42] G. Lota, E. Frackowiak, Striking capacitance of carbon/iodide interface, Electrochem. Commun. 11 (2009) 87–90.
[43] G. Lota, K. Fic, E. Frackowiak, Alkali metal iodide/carbon interface as a source of pseudocapacitance, Electrochem. Commun. 12 (2011) 38–41.
[44] S.T. Senthilkumar, R. Kalai Selvan, Y.S. Lee, J.S. Melo, Electric double layer capacitor and its improved specific capacitance using redox additive electrolyte, J. Mater. Chem. A 1 (2013) 1086–1095.
[45] D. Jain, J. Kanungo, S.K. Tripathi, Enhanced performance of ultracapacitors using redox additive-based electrolytes, Appl. Phys. A Mater. Sci. Process. 124 (2018) 397.
[46] D. Xu, W. Hu, X.N. Sun, P. Cui, X.Y. Chen, Redox additives of Na_2MoO_4 and KI: synergistic effect and the improved capacitive performances for carbon-based supercapacitors, J. Power Sources 341 (2017) 448–456.
[47] K. Jayaramulu, D.P. Dubal, B. Nagar, V. Ranc, O. Tomanec, M. Petr, K.K.R. Datta, R. Zboril, P.G. Romero, R.A. Fischer, Ultrathin hierarchical porous carbon nanosheets for high-performance supercapacitors and redox electrolyte energy storage, Adv. Mater. (2018) 1705789.
[48] T. Otowa, R. Tanibata, M. Itoh, Production and adsorption characteristics of MAXSORB: high-surface-area active carbon, Gas Sep. Purif. 7 (1993) 241–245.
[49] D. Lozano-Castello, J.M. Calo, D. Cazorla-Amoros, A. Linares-Solano, Carbon activation with KOH as explored by temperature programmed techniques, and the effects of hydrogen, Carbon 45 (2007) 2529–2536.
[50] J. Wang, S. Kaskel, KOH activation of carbon-based materials for energy storage, J. Mater. Chem. 22 (2012) 23710–23725.
[51] A. Swiatkowski, A. Dabrowski, Studies in Surface Science and Catalysis, 120, Part A Elsevier, 1999, p. 69.
[52] M. Zeiger, N. Jackel, V.N. Mochalin, V. Presser, Review: carbon onions for electrochemical energy storage, J. Mater. Chem. A 4 (2016) 3172–3196.
[53] Z. Xu, X. Zhuang, C. Yang, J. Cao, Z. Yao, Y. Tang, J. Jiang, D. Wu, X. Feng, Nitrogen-doped porous carbon superstructures derived from hierarchical assembly of polyimide nanosheets, Adv. Mater. 28 (2016) 1981–1987.
[54] F. Cheng, W. Liu, Y. Zhang, H. Wang, S. Liu, E. Hao, S. Zhao, H. Yang, Squid inks-derived nano carbons with unique “shell@pearls” structure for high-performance supercapacitors, J. Power Sources 354 (2017) 116–123.
[55] T. Ranjith, K. Karthikeyan, R.H. Vignesh, X. Sun, Y.-S. Lee, Engineering the pores of biomass-derived carbon: insights for achieving ultrahigh stability at high power in high-energy supercapacitors, ChemSusChem. 10 (2017) 2805–2815.
[56] C. Largeot, C. Portet, J. Chmiola, P.-L. Taberna, Y. Gogotsi, P. Simon, Relation between the ion size and pore size for an electric double-layer capacitor, J. Am. Chem. Soc. 130 (2008) 2730–2731.
[57] J. Sodtipinta, C. Ieosakulrat, N. Poonyayant, P. Kidkhunthod, N. Chanlek, T. Amornsakchai, Pasit Pakawatpanurut, Interconnected open-channel carbon nanosheets derived from pineapple leaf fiber as a sustainable active material for supercapacitors, Ind. Crop. Prod. 104 (2017) 13–20.
[58] R. Kalai Selvan, P. Zhu, C. Yan, J. Zhu, M. Dirican, A. Shanmugavani, Y.S. Lee, X. Zhang, Biomass-derived porous carbon modified glass fiber separator as polysulfide reservoir for Li-S batteries, J. Colloid Interface Sci. 513 (2018) 231–239.
[59] Y. Liu, J.S. Xue, T. Zheng, J.R. Dahn, Mechanism of lithium insertion in hard carbons prepared by pyrolysis of epoxy resin, Carbon 34 (1996) 193–200.
[60] D. Qu, Investigation of hydrogen physisorption active sites on the surface of porous carbonaceous materials, Chemistry 14 (2008) 1040–1046.
[61] H. Wang, Q. Gao, J. Hu, High hydrogen storage capacity of porous carbons prepared by using activated carbon, J. Am. Chem. Soc. 131 (2009) 7016–7022.
[62] J.K. McDonough, Y. Gogotsi, Carbon onions: synthesis and electrochemical applications, Electrochem. Soc. Interface Fall. 22 (2013) 61–66.
[63] S.L.H. Rebelo, A. Guedes, M.E. Szefczyk, A.M. Pereira, J.P. Araujo, C. Freire, Progresses on the Raman spectra analysis of covalently functionalized multiwall carbon nanotubes: unravelling disorder on graphitic materials, Phys. Chem. Chem. Phys. 18 (2016) 12784–12796.
[64] M.A. Pimenta, G. Dresselhaus, M.S. Dresselhaus, L.G. Canç, A. Jorioa, R. Saitoe,

Studying disorder in graphite-based systems by Raman spectroscopy, Phys. Chem. Chem. Phys. 9 (2007) 1276–1291.
[65] R. Bajpai, S. Roy, N. Kulshrestha, J. Rafiee, N. Koratkar, D.S. Misra, Graphene supported nickel nanoparticle as a viable replacement for platinum in dye sensitized solar cells, Nanoscale 4 (2012) 926–930.
[66] D.C. Pujals, O.A. de Fuentes, L.F.D. Garcia, E. Cazzanelli, L.S. Caputi, Raman spectroscopy of polyhedral carbon nano-onions, Appl. Phys. A Mater. Sci. Process. 120 (2015) 1339–1345.
[67] H. Lee, M.A. Bratescu, T. Ueno, N. Saito, Solution plasma exfoliation of graphene flakes from graphite electrodes, RSC Adv. 4 (2014) 51758–51765.
[68] K. Pandi, K.V. Sankar, D. Kalpana, Y.S. Lee, R. Kalai Selvan, Fabrication of solid-state flexible fiber supercapacitor using agave Americana derived activated carbon and its performance analysis at different conditions, Chemistry Select 1 (2016) 6713–6725.
[69] Y. Chen, Q. Liu, J. Wang, Highly porous nitrogen-doped carbon nanofibers as efficient metal-free catalysts toward the electrocatalytic oxygen reduction reaction, Nano Adv. 1 (2016) 79–89.
[70] M. Dhelipan, A. Arunchander, A.K. Sahu, D. Kalpana, Activated carbon from orange peels as supercapacitor electrode and catalyst support for oxygen reduction reaction in proton exchange membrane fuel cell, J Saudi Chem Soc 21 (2017) 487–494.
[71] N. Sudhan, K. Subramani, M. Karnan, N. Ilayaraja, M. Sathish, Biomass-derived activated porous carbon from rice straw for a high-energy symmetric supercapacitor in aqueous and nonaqueous electrolytes, Energy Fuel 31 (2017) 977–985.
[72] J. Romanos, M. Beckner, T. Rash, L. Firlej, B. Kuchta, P. Yu, G. Suppes, C. Wexler, P. Pfeifer, Nanospace engineering of KOH activated carbon, Nanotechnology 23 (2012) 015401.
[73] M. Zhu, J. Lan, X. Zhang, G. Sui, X. Yang, Porous carbon derived from Ailanthus altissima with unique honeycomb-like microstructure for high-performance supercapacitors, New J. Chem. 41 (2017) 4281–4285.
[74] X.-F. Wu, S.-X. Li, M.-F. Li, Effect of temperature on the properties of charcoal prepared from carbonization of biorefinery lignin, Bioresources 13 (2018) 6736–6745.
[75] J. Wang, I. Senkovsk, M. Oschatz, M.R. Lohe, L. Borchardt, A. Heerwig, Q. Liu, S. Kaskel, Highly porous nitrogen-doped polyamine-based carbons with adjustable microstructures for CO_2 capture, J. Mater. Chem. A 1 (2013) 10951–10961.
[76] H.D. Yoo, J.H. Jang, J.H. Ryu, Y. Park, S.M. Oh, Impedance analysis of porous carbon electrodes to predict rate capability of electric double-layer capacitors, J. Power Sources 267 (2014) 411–420.
[77] S.T. Senthilkumar, R. Kalai Selvan, N. Ponpandian, J.S. Melo, Redox additive aqueous polymer gel electrolyte for an electric double layer capacitor, RSC Adv. 2 (2012) 8937–8940.
[78] B.E. Conway, Electrochemical Supercapacitor, Kluwer Academic/Plenum Publisher, New York, 1999.
[79] J.R. Miller, Proceedings of the 8th International Seminar on Double-layer Capacitors and Similar Energy Storage Devices, Deerfield Beach, Florida, December 7–9 (1998).
[80] Z. Niu, H. Dong, B. Zhu, J. Li, H.H. Hng, W. Zhou, X. Chen, S. Xie, Highly stretchable, integrated supercapacitors based on single-walled carbon nanotube films with continuous reticulate architecture, Adv. Mater. 25 (2013) 1058–1064.
[81] D. Jain, J. Kanungo, S.K. Tripathi, Performance enhancement approach for supercapacitor by using mango kernels derived activated carbon electrode with p-hydroxy aniline based redox additive electrolyte, Mater. Chem. Phys. 229 (2019) 66–77.
[82] M. Tian, J. Wu, R. Li, Y. Chen, D. Long, Fabricating a high-energy-density supercapacitor with asymmetric aqueous redox additive electrolytes and free-standing activated-carbon-felt electrodes, Chem. Eng. Sci. 363 (2019) 183–191.
[83] K. Sun, Z. Zhang, H. Peng, G. Zhao, G. Ma, Z. Leib, Hybrid symmetric supercapacitor assembled by renewable corn silks based porous carbon and redox-active electrolytes, Mater. Chem. Phys. 218 (2018) 229–238.
[84] Y. Wang, Z. Chang, M. Qian, Z. Zhang, J. Lin, F. Huang, Enhanced specific capacitance by a new dual redox-active electrolyte in activated carbon-based supercapacitors, Carbon 143 (2019) 300–308.
[85] Y.-C. Chen, L.-Y. Lin, Investigating the redox behavior of activated carbon supercapacitors with hydroquinone and p-phenylenediamine dual redox additives in the electrolyte, J. Colloid Interface Sci. 537 (2019) 295–305.
[86] Z.J. Zhang, J.X. Li, T.T. Huang, M.R. Liu, X.Y. Chen, Large performance improvement of carbon-based supercapacitors using dual-redox additives phosphotungstic acid and potassium ferricyanide, J Alloy Compd 768 (2018) 756–765.
[87] Q. Sun, Y. Li, T. He, The excellent capacitive capability for N, P-doped carbon microsphere/reduced graphene oxide nanocomposites in H_2SO_4/KI redox electrolyte, J. Mater. Sci. 54 (2019) 7665–7678.
[88] C. Xia, M. Leng, W. Tao, Q. Wang, Y. Gao, Q. Zhang, Polyaniline/carbon nanotube core–shell hybrid and redox active electrolyte for high-performance flexible supercapacitor, J. Mater. Sci. Mater. Electron. 30 (2019) 4427–4436.